

Article

Fault Diagnosis Method of Six-Phase Permanent Magnet Synchronous Motor Based on Vector Space Decoupling

Hanying Gao *, Jie Guo, Zengquan Hou, Bangping Zhang and Yao Dong

School of Electrical and Electronic Engineering, Harbin University of Science and Technology, Harbin 150080, China; 1603011307@stu.hrbust.edu.cn (J.G.); 1920310189@stu.hrbust.edu.cn (Z.H.); zbp123456@163.com (B.Z.); a1090897186@163.com (Y.D.)

* Correspondence: ghy@hrbust.edu.cn; Tel.: +86-137-9666-8369

Abstract: Compared with the three-phase motor, the six-phase motor has lower torque ripple and higher fault tolerance performance, which makes it widely used in aviation, ships, industrial manufacturing, and other application fields. However, the probability of failure of the polyphase motor system increases with the increase in the number of phases. In order to deal with the open phase fault and power switch fault of the six-phase inverter, a fault diagnosis method for the six-phase inverter based on vector space decoupling (VSD) is proposed. The open phase fault index is first determined according to the VSD decoupling inverse transform and the current constraints. The fault index is then optimized from the perspective of preventing misdiagnosis and improving reliability, and the open phase fault can be diagnosed in one fundamental cycle. In addition, the current trajectory of harmonic plane after switch fault is analyzed, and the back propagation (BP) neural network is used to identify the harmonic plane current trajectory of different types of switch fault. Finally, the correctness and feasibility of the proposed fault diagnosis method are verified by simulations and experiments. The obtained results demonstrate that the proposed method can quickly and accurately locate the open phase fault and switch fault without additional hardware. The proposed method is simple, efficient, and robust.

Keywords: six-phase permanent magnet synchronous motor (PMSM); inverter fault diagnosis; neural network; open circuit fault; power switch failure



Citation: Gao, H.; Guo, J.; Hou, Z.; Zhang, B.; Dong, Y. Fault Diagnosis Method of Six-Phase Permanent Magnet Synchronous Motor Based on Vector Space Decoupling. *Electronics* **2022**, *11*, 1229. <https://doi.org/10.3390/electronics11081229>

Academic Editor: Ahmed Abu-Siada

Received: 21 March 2022

Accepted: 7 April 2022

Published: 13 April 2022

Publisher's Note: MDPI stays neutral with regard to jurisdictional claims in published maps and institutional affiliations.



Copyright: © 2022 by the authors. Licensee MDPI, Basel, Switzerland. This article is an open access article distributed under the terms and conditions of the Creative Commons Attribution (CC BY) license (<https://creativecommons.org/licenses/by/4.0/>).

1. Introduction

The polyphase permanent magnet synchronous motor has its unique advantages in improving power, restraining torque ripple, and fault-tolerant control. It is suitable for ships [1], aerospace [2], energy utilization [3], rail transit [4], and other application domains with high-reliability requirements. However, compared with the three-phase motor, the number of power devices and sensors in the driving system of the polyphase motor is also doubled. In the case of failure, it will threaten personal safety or lead to system collapse. Therefore, it is necessary to detect and diagnose the different operating parameters in the early stage of system fault.

In the polyphase motor drive system, the inverter switch failure and phase failure rate are the highest [5]. The fault diagnosis technology can instantly and accurately locate the fault location of the motor drive system and provide key information for maintenance and repair. In addition, it provides an accurate basis for the selection of the subsequent fault-tolerant control technology of the polyphase motor. Therefore, a fast, stable, and accurate fault diagnosis method for polyphase motor drive systems is crucial.

Three main fault diagnosis methods for motor drive systems exist: model-based [6–8], knowledge-based [9,10], and signal-based [11]. In [12], the related terms of DC side voltage and current of inverter are modeled and analyzed, and the residual evaluation function of DC side voltage is constructed to diagnose the fault of switch. A phase current observer

is designed to convert the phase current error into coordinates to obtain the fault vector angle, so as to locate the switch fault [13]. A current interval sliding mode observer is designed to improve the prediction process of the phase current [14]. The performance of the model-based fault diagnosis method highly depends on the model's accuracy. The changes in the motor parameters and operating conditions will also have a certain impact on the diagnosis accuracy.

In the knowledge-based diagnosis method, the main neural network algorithm and auxiliary neural network are used to analyze the amplitude-frequency characteristics of DC bus voltage harmonics and diagnose the fault of the three-level inverter power device [15]. In [16], the intermittent faults of power equipment are studied, and the fault levels under different fault conditions are classified by using fuzzy theory. In [17], a new method is mentioned to diagnose the fault of a wind turbine by developing a knowledge base to simulate the thinking mode of experts. This method has a high computational load, and low real-time performance, and it is difficult to implement.

The fault diagnosis based on signals can be divided into voltage and current methods. The typical shape of the fault track is matched by calculating the distance from the harmonic plane current track to the centroid [18]. This algorithm is complex and requires a lot of calculations. In [19], a new method is mentioned to decompose and reconstruct the voltage signal by using wavelet packets. It also uses the characteristic frequency related to the fault signal in its power spectrum to judge the open circuit fault type of the switch. In [20], by analyzing the frequency and angle of each current vector, whether the power switch of the three-phase inverter fails can be judged. In [21], the sampled current is decomposed using the wavelet transform and transformed by coordinate, and the fault trajectory is diagnosed using the support vector machine.

In this paper, a fault diagnosis method based on VSD is proposed for phase failure and power switch failure. The phase failure index is first determined according to the VSD transformation and phase failure constraints. A series of fault indexes are then optimized in order to improve the diagnosis reliability. Afterward, the switch fault is diagnosed as the characteristic signal by analyzing the current trajectories of harmonic planes after VSD transformation. Finally, considering the 10 kW double Y-phase shifted 30° six-phase PMSM, the correctness of the diagnosis algorithm is verified by simulations and experiments.

2. Mathematical Model of the Six-Phase Permanent Magnet Synchronous Motor

The six-phase PMSM drive system is mainly composed of a six-phase voltage source inverter (VSI). Its topology is shown in Figure 1. Note that N1 and N2 are the neutral points of the two windings.

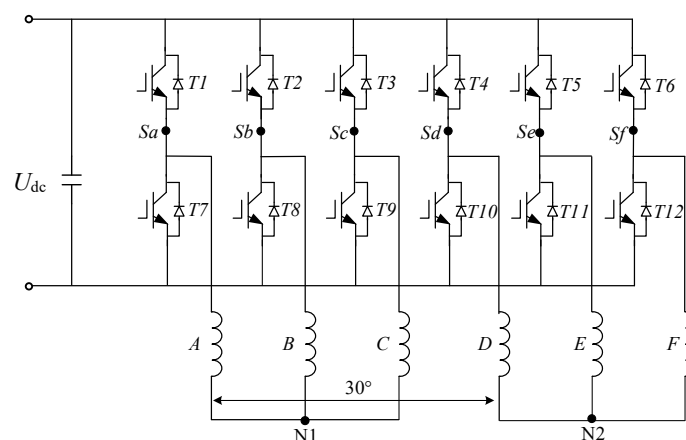


Figure 1. Topology of the six-phase inverter with neutral isolation.

The six-phase PMSM is a nonlinear and strongly coupled system. Therefore, an appropriate decoupling transformation is required to simplify the analysis. In addition, the VSD

decoupling method, which is more suitable for polyphase motors, can control the harmonic component. The vector space decoupling matrix is given by:

$$C_{6s} = \frac{1}{\sqrt{3}} \begin{bmatrix} 1 & -\frac{1}{2} & -\frac{1}{2} & \frac{\sqrt{3}}{2} & -\frac{\sqrt{3}}{2} & 0 \\ 0 & \frac{\sqrt{3}}{2} & -\frac{\sqrt{3}}{2} & \frac{1}{2} & \frac{1}{2} & -1 \\ 1 & -\frac{1}{2} & -\frac{1}{2} & -\frac{\sqrt{3}}{2} & \frac{\sqrt{3}}{2} & 0 \\ 0 & -\frac{\sqrt{3}}{2} & \frac{\sqrt{3}}{2} & \frac{1}{2} & \frac{1}{2} & -1 \\ 1 & 1 & 1 & 0 & 0 & 0 \\ 0 & 0 & 0 & 1 & 1 & 1 \end{bmatrix} \quad (1)$$

In this matrix, the first two rows of variables correspond to the α - β subspace, the middle two rows correspond to the z_1 - z_2 subspace, and the last two rows correspond to the o_1 - o_2 zero sequence. The conversion of electromechanical energy is only related to α - β .

The rotation coordinate transformation is expressed as:

$$C_{6s/6r} = \begin{bmatrix} \cos \theta & \sin \theta & 0 \\ -\sin \theta & \cos \theta & 0 \\ 0 & 0 & I_4 \end{bmatrix} \quad (2)$$

where I_4 is a fourth-order unit matrix. The motor mathematical model after VSD transformation is detailed in the sequel.

The magnetic flux equation is:

$$\begin{bmatrix} \psi_d \\ \psi_q \end{bmatrix} = \begin{bmatrix} L_d & 0 \\ 0 & L_q \end{bmatrix} \begin{bmatrix} i_d \\ i_q \end{bmatrix} + \psi_f \begin{bmatrix} 1 \\ 0 \end{bmatrix} \quad (3)$$

where L_d and L_q , i_d and i_q , ψ_d and ψ_q are the inductance, current, and stator flux of the direct axis and quadrature axis, respectively.

The voltage equation is:

$$\begin{bmatrix} u_d \\ u_q \end{bmatrix} = \begin{bmatrix} R & 0 \\ 0 & R \end{bmatrix} \begin{bmatrix} i_d \\ i_q \end{bmatrix} + \frac{d}{dt} \begin{bmatrix} \psi_d \\ \psi_q \end{bmatrix} + \omega_e \begin{bmatrix} -\psi_q \\ \psi_d \end{bmatrix} \quad (4)$$

where u_d and u_q are the stator voltages of the direct axis and quadrature axis, respectively.

The electromagnetic torque equation is:

$$T_e = 3p[\psi_f i_q + (L_d - L_q)i_d i_q] \quad (5)$$

where T_e and ψ_f are the electromagnetic torque and permanent magnet flux linkage, respectively.

The equation of motion is:

$$T_e - T_L - B\omega_m = J \frac{d\omega_m}{dt} \quad (6)$$

where T_L , B , ω_m , and J are load torque, damping coefficient, mechanical angular velocity, and moment of inertia, respectively.

3. Open Phase Fault Diagnosis Strategy

After VSD transformation, the property of the α - β plane variable is similar to that of the three-phase motor, while the z_1 - z_2 plane is a unique property of the six-phase PMSM [22]. Simultaneously, the change of the z_1 - z_2 component during inverter fault is explored, which can be used for inverter fault diagnosis.

3.1. Calculation of the Phase Failure Index

In the normal state, the fundamental subspace current i_α, i_β in the VSD static coordinate system is obtained by decoupling transformation of the six-phase stator current:

$$i_\alpha = i_a - \frac{1}{2}i_b - \frac{1}{2}i_c + \frac{\sqrt{3}}{2}i_d - \frac{\sqrt{3}}{2}i_e \tag{7}$$

$$i_\beta = \frac{\sqrt{3}}{2}i_b - \frac{\sqrt{3}}{2}i_c + \frac{1}{2}i_d + \frac{1}{2}i_e - i_f \tag{8}$$

Substituting the six-phase stator current of the motor during normal operation into Equations (7) and (8), the following is obtained:

$$\begin{cases} i_\alpha = I_m \sin(\theta) - \frac{1}{2}I_m \sin(\theta - \frac{2\pi}{3}) - \frac{1}{2}I_m \sin(\theta + \frac{2\pi}{3}) + \frac{\sqrt{3}}{2}I_m \sin(\theta - \frac{\pi}{6}) - \frac{\sqrt{3}}{2}I_m \sin(\theta - \frac{5\pi}{6}) = 3I_m \sin(\theta) \\ i_\beta = \frac{\sqrt{3}}{2}I_m \sin(\theta - \frac{2\pi}{3}) - \frac{\sqrt{3}}{2}I_m \sin(\theta + \frac{2\pi}{3}) + \frac{1}{2}I_m \sin(\theta - \frac{\pi}{6}) + \frac{1}{2}I_m \sin(\theta - \frac{5\pi}{6}) - I_m \sin(\theta + \frac{\pi}{6}) = 3I_m \cos(\theta) \end{cases} \tag{9}$$

Similarly, the current relationship in the harmonic subplane can be obtained:

$$\begin{cases} i_x = i_a - \frac{1}{2}i_b - \frac{1}{2}i_c - \frac{\sqrt{3}}{2}i_d + \frac{\sqrt{3}}{2}i_e \\ i_y = -\frac{\sqrt{3}}{2}i_b + \frac{\sqrt{3}}{2}i_c + \frac{1}{2}i_d + \frac{1}{2}i_e - i_f \end{cases} \tag{10}$$

Substituting the six-phase stator current of the motor during normal operation into Equation (10) results in:

$$\begin{cases} i_x = 0 \\ i_y = 0 \end{cases} \tag{11}$$

It can be deduced from this analysis that the output electromagnetic torque of the motor is mainly provided by the fundamental subspace current components i_α and i_β . In the normal state, the current i_{z1}, i_{z2} of the harmonic subplane is null. The currents i_α, i_β and i_{z1}, i_{z2} after VSD decoupling transformation are shown in Figure 2. The fundamental subspace is circular in the steady-state current i_α, i_β . The harmonic subspace current i_{z1}, i_{z2} is the point at the origin, which is coherent with the theoretical calculation results.

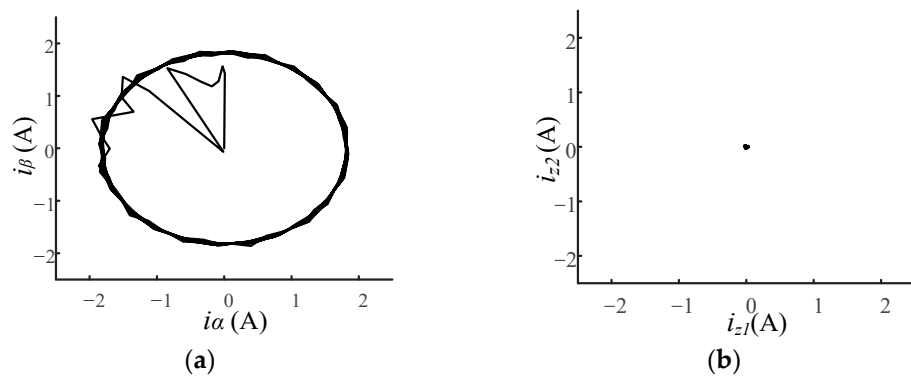


Figure 2. α - β and z_1 - z_2 plane current waveform during normal operation: (a) α - β plane current waveform in case of normal operation; (b) z_1 - z_2 plane current waveform in case of normal operation.

By inverting the normal VSD transformation, the following is obtained:

$$\begin{bmatrix} i_a \\ i_b \\ i_c \\ i_d \\ i_e \\ i_f \end{bmatrix} = \frac{1}{\sqrt{3}} \begin{bmatrix} 1 & 0 & 1 & 0 & 1 & 0 \\ -\frac{1}{2} & \frac{\sqrt{3}}{2} & -\frac{1}{2} & -\frac{\sqrt{3}}{2} & 1 & 0 \\ -\frac{1}{2} & -\frac{\sqrt{3}}{2} & -\frac{1}{2} & \frac{\sqrt{3}}{2} & 1 & 0 \\ \frac{\sqrt{3}}{2} & \frac{1}{2} & -\frac{\sqrt{3}}{2} & \frac{1}{2} & 0 & 1 \\ -\frac{\sqrt{3}}{2} & \frac{1}{2} & \frac{\sqrt{3}}{2} & 0 & 0 & 1 \\ 0 & -1 & 0 & -1 & 0 & 1 \end{bmatrix} \begin{bmatrix} i_\alpha \\ i_\beta \\ i_{z1} \\ i_{z2} \\ i_{o1} \\ i_{o2} \end{bmatrix} \tag{12}$$

When a phase failure occurs, it can be seen from Equation (12) that the fundamental and harmonic plane currents have a certain relationship. It is assumed that the phase failure of phase a winding occurs. That is, when the constraint condition is $i_a = 0$, the first row of the VSD inverse matrix (cf. Equation (12)) is multiplied by the plane current in order to obtain $i_\alpha + i_{z1} = 0$. When the motor is in normal operation, the harmonic current is $i_{z1} = 0$. In summary, the open circuit fault index F_a can be computed as:

$$F_a = -\frac{i_{z1}}{i_\alpha} \tag{13}$$

Similarly, the open-circuit fault index of six-phases (cf. Equation (14)) can be obtained:

$$\left\{ \begin{array}{l} F_a = -\frac{i_{z1}}{i_\alpha} \\ F_b = \frac{i_{z1}}{-i_a + \sqrt{3}i_\beta - \sqrt{3}i_{z2}} \\ F_c = \frac{i_{z1}}{-i_a - \sqrt{3}i_\beta + \sqrt{3}i_{z2}} \\ F_d = \frac{i_{z1}}{i_a + 1/\sqrt{3}i_\beta + 1/\sqrt{3}i_{z2}} \\ F_e = \frac{i_{z1}}{i_a - 1/\sqrt{3}i_\beta - 1/\sqrt{3}i_{z2}} \\ F_f = -\frac{i_{z2}}{i_\beta} \end{array} \right. \tag{14}$$

The numerator of this fault index is the harmonic plane current. Due to the fact that the harmonic plane current component is null in the normal state, the fault index is always kept null during the normal operation of the motor. When a phase fault occurs, the fault index of the phase rises 1, so as to distinguish the normal operation and inverter phase fault.

3.2. Optimization Scheme of the Winding Open Circuit Fault Index

In the case where only the fault index F_n ($n = a, b, c, d, e, f$) is used, because the denominator of the fault indicator is too small near the zero-crossing area, a spike pulse will appear, which may lead to misdiagnosis. Therefore, the fault index F_n should be improved and optimized. The optimization process is illustrated in Figure 3.

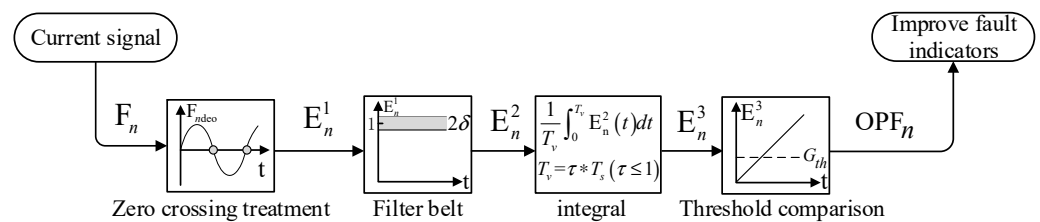


Figure 3. Fault index optimization process of disconnected phase.

The fault index F_n is first subjected to peak pulse processing using Equation (15), in order to obtain the first fault index E_n^1 :

$$\left\{ \begin{array}{l} E_n^1 = 0, |F_{nde0}| \leq \Delta \\ E_n^1 = F_n, |F_{nde0}| > \Delta \end{array} \right. \tag{15}$$

where F_{nde0} is the denominator value of fault index F_n and Δ is the threshold value of the zero-crossing area width. This value cannot be too large, in order to ensure the diagnosis speed. The specific value is determined according to the experiment. In this paper, Δ is set to 0.1.

The fault index after peak pulse processing is then filtered using Equation (16) in order to obtain the second fault index E_n^2 :

$$\left\{ \begin{array}{l} E_n^2 = E_n^1, (1 - \delta \leq E_n^1 \leq 1 + \delta) \\ E_n^2 = 0, (1 + \delta \leq E_n^1 \& E_n^1 \leq 1 - \delta) \end{array} \right. \tag{16}$$

where δ is the width of the filter band, which is used to filter out the unnecessary interference while not affecting the subsequent processing. The recommended value range of δ is [0.1–0.3]. In this paper, it is set to 0.1.

The processed fault index will be set to 1 after the fault occurs. However, the fault index will be set to zero in the zero-crossing area, due to the processing of the zero-crossing spike pulse. Therefore, it is necessary to integrate the fault index according to Equation (17) in order to obtain the third fault index E_n^3 :

$$E_n^3 = \frac{1}{T_v} \int_0^{T_v} E_n^2(t) dt \quad (17)$$

$$T_v = \tau * T_s (\tau \leq 1) \quad (18)$$

where T_s is the periodic value of the current fundamental wave. The larger the value of τ , the slower the diagnosis speed, but the higher the diagnosis accuracy. On the contrary, the smaller the value of τ , the faster the diagnosis speed, but the smaller the diagnosis accuracy. In this paper, τ is set to 0.6, in order to ensure the diagnosis accuracy and rapidity. The traditional integration consists in integrating the fault indicators of the whole cycle, which will prolong the fault diagnosis time and reduce the diagnosis efficiency. Selecting T_v Equation (18) can speed up the detection speed.

Finally, the third fault index E_n^3 is compared with the threshold in order to obtain the improved fault index OPF_n :

$$\begin{cases} OPF_n = 1, E_n^3 > G_{th} \\ OPF_n = 0, E_n^3 < G_{th} \end{cases} \quad (19)$$

where G_{th} is the judgment threshold selected between 0 and 1. If the value of G_{th} is too large, the diagnosis speed will slow down. Because these steps have a negative integration link to suppress the fluctuation of fault indicators, the value can be appropriately reduced, and G_{th} can have a value between 0.1 and 0.3.

It can be deduced that using the constraint condition that the fault phase current is null after the phase failure, combined with the vector space decoupled VSD inverse matrix, the fault index of the phase failure is derived. This can diagnose and locate 15 types of phase faults of the inverter, including 6 types of single-phase faults and 9 types of two-phase faults of different windings.

4. Power Switch Fault Diagnosis Strategy

Several types of power switch faults exist. They mainly include the short circuit and open circuit faults. The short circuit fault has a short duration and is difficult to detect. For further treatment, the short circuit fault is changed into open an circuit fault by a fuse device. The open-circuit faults are mostly single-switch and two-switch faults. The fault of two switches on the same bridge arm can be treated as open phase fault. Therefore, this paper only tackles the open circuit fault of a single switch and two switches on different bridge arms.

4.1. Harmonic Plane Current Fault Trace Analysis

Figure 4 shows the current waveform of the z_1 - z_2 plane when different switches fail after VSD conversion of the six-phase stator current. When T1 fails, the current trajectory of the z_1 - z_2 plane points to the negative half of the z_1 axis. When T1 and T2 fail, the current trajectories of i_{z1} and i_{z2} are fan-shaped. Similarly, when other switches fail, they also have these trajectory characteristics.

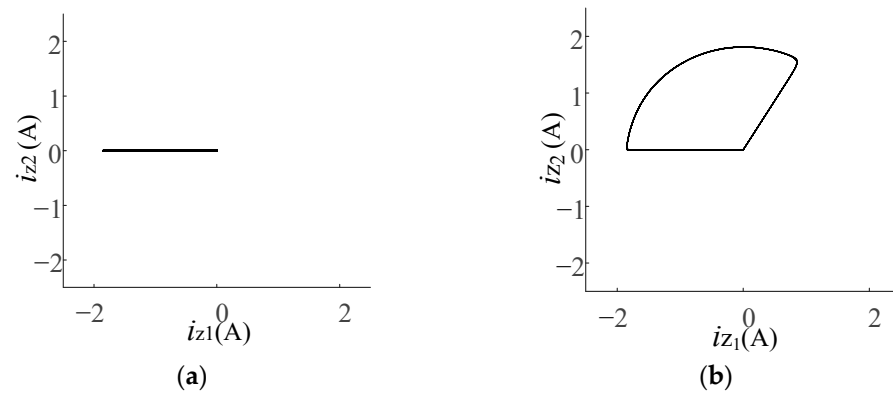


Figure 4. z_1 - z_2 plane current in case of different power switch faults; (a) z_1 - z_2 plane current waveform in case of T1 fault; (b) z_1 - z_2 plane current waveform in case of T1 and T2 faults.

The reference direction of the current vector during each phase fault can be expressed as:

$$\text{dn} - \text{ref} = \arctan\left(\frac{A_{z2}}{A_{z1}}\right) \begin{cases} \pi - (k - 1)\frac{\pi}{6}, f_n \leq 1 \\ -(k - 1)\frac{\pi}{6}, f_n \geq 0 \end{cases} \quad (20)$$

where A_{z1} and A_{z2} represent the amplitude of harmonic currents i_{z1} and i_{z2} , respectively. n represents the a, b, c, d, e, f phase, while the fault phase corresponding to $k = 1, 5, -3, -4, 6, 4$ is a, b, c, d, e, f , respectively. The fault current vector turns counterclockwise by angle dn-ref from the x axis. $f_n(t) = \int_0^T i_n dt$ is the average value of fault current in a current cycle.

It can be deduced that in the case of a single-switch or two-switch open-circuit fault of the inverter, the current trajectory in the harmonic i_{z1} and i_{z2} planes regularly changes. The current vector trajectory profile under single-switch and multi-switch faults can be developed using the current values in the i_{z1} and i_{z2} harmonic planes, as shown in Figures 5 and 6.

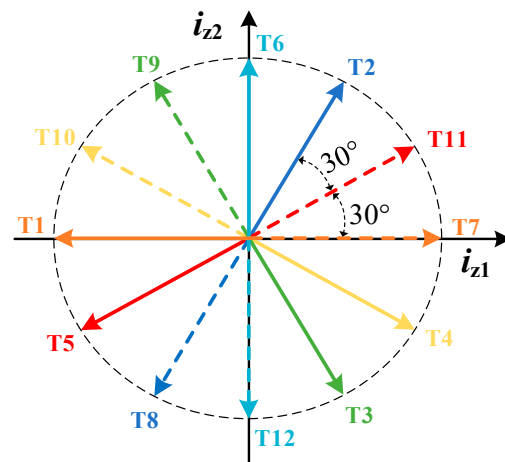


Figure 5. Reference direction of i_{z1} and i_{z2} current trace in the case of a single switch failure.

According to the different reference directions of the current track under the z_1 - z_2 plane fault, the intelligent algorithm has the characteristics of strong analysis ability and several diagnosis types. Therefore, the neural network algorithm is used for fault diagnosis based on the characteristics of fault current trajectory.

In order to distinguish the fault types and improve the diagnosis efficiency, different fault types should be classified and coded. The 12 bit binary number $F_1F_2F_3F_4F_5F_6F_7F_8F_9F_{10}F_{11}F_{12}$ is used to encode the single-switch and two-switch faults of the six-phase inverter. When all the bits are equal to 1, the switch has an open-circuit fault. On the contrary, when all the

bits are 0, the switch has no fault. Note that there are 36 fault conditions. The specific fault types are shown in Table 1.

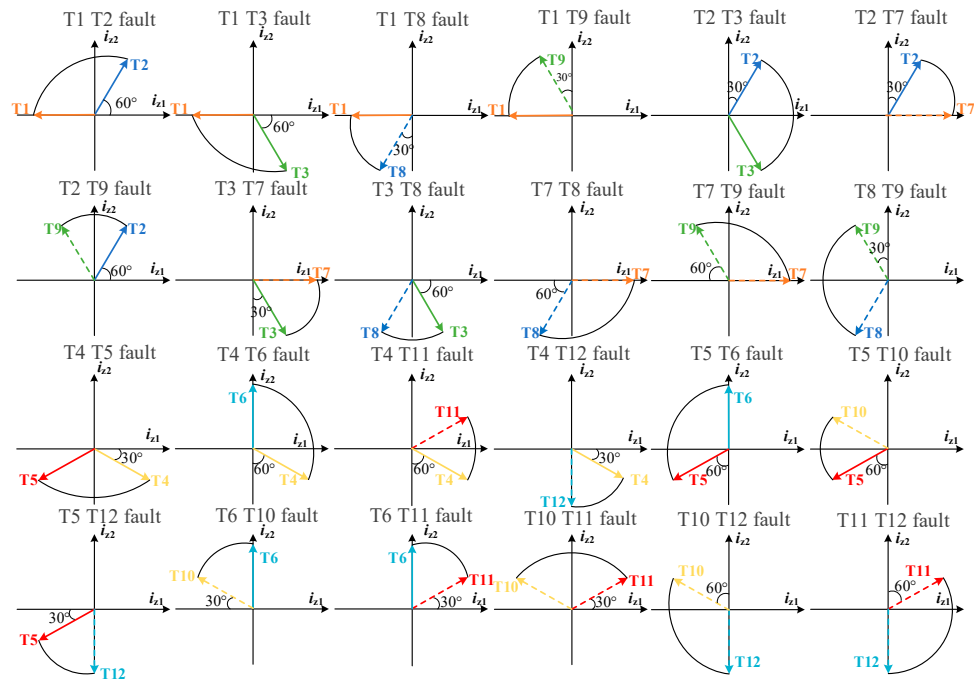


Figure 6. Reference direction of i_{z1} and i_{z2} current trace, in the case of two-power-switch faults.

Table 1. Fault type code.

Fault Switch	Fault Type	Fault Code	Fault Switch	Fault Type	Fault Code
Nothing	Normal	000000000000			
T1	Single-switch fault of the first set of winding	100000000000	T4	Failure of two switches of the second set of winding	000110000000
T2		010000000000	T5		000010000000
T3		001000000000	T6		000001000000
T7		000000100000	T10		000000000100
T8		000000010000	T11		000000000010
T9		000000001000	T12		000000000001
T1T2		110000000000	T4T5		000110000000
T1T3		101000000000	T4T6		000101000000
T1T8		100000010000	T4T11		000100000010
T1T9	100000001000	T4T12	000100000001		
T2T3	011000000000	T5T6	000011000000		
T2T7	010000100000	T5T10	000010000100		
T2T9	010000001000	T5T12	000010000001		
T3T7	001000100000	T6T10	000001000100		
T3T8	001000001000	T6T11	000001000010		
T7T8	000000110000	T10T11	000000000110		
T7T9	000000010100	T10T12	000000000101		
T8T9	000000001100	T11T12	000000000011		

4.2. Principle and Algorithm of BP Neural Network

The neural network is a nonlinear system. Each neuron can output a signal according to the input layer signal and activation system function. In addition, a large number of neurons can jointly form a highly nonlinear system [23]. Figure 7 presents a representative neuron structure model.

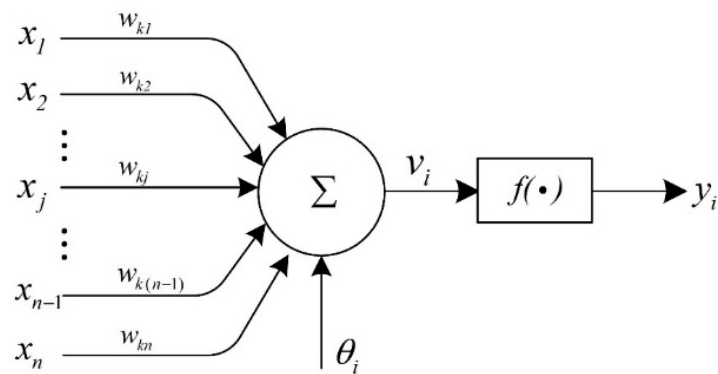


Figure 7. Single neuron structure.

In the latter, $x_1, x_2, x_3 \dots x_n$ is the input parameter, $W_{k1}, W_{k2}, W_{k3} \dots W_{k(n-1)}, W_{kn}$ represents the weight of each parameter, θ_i denotes the threshold, $f(\cdot)$ s the activation function, and y_i represents the neuron output. The relationship between each variable is given by:

$$\begin{cases} u_i = \sum_{j=1}^n w_{ij}x_j \\ v_i = u_i + \theta \end{cases} \tag{21}$$

The output y_i of the neuron is expressed as:

$$y_i = f\left(\sum_{j=1}^n w_{ij}x_j + \theta_i\right) \tag{22}$$

The structure of the BP neural network is shown in Figure 8. Due to the gradient descent method, the training can fall into the local minimum, which leads to the inability of effective training [24]. Therefore, this paper uses the Levenberg–Marquardt algorithm based on the combination of the gradient method and Newton method, in order to optimize the BP neural network. This method has less iterations and a fast iteration speed. Therefore, it can approach the optimal weight faster in order to complete the training.

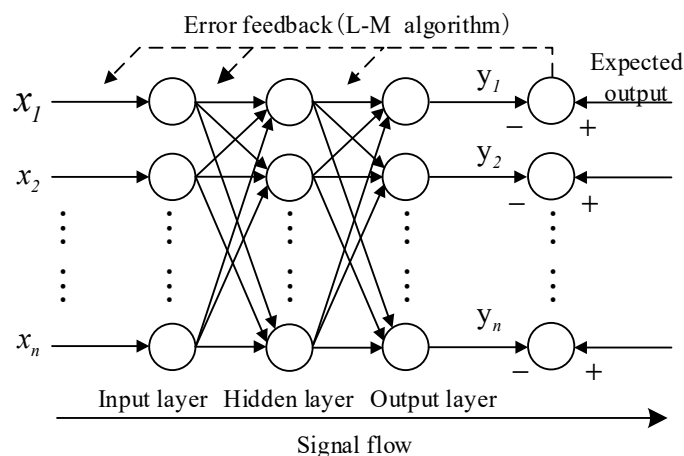


Figure 8. Neural network structure model.

Considering that the residual of the output layer is $\gamma(x)$, which has a nonlinear relationship with x , the iterative formula of the Gauss Newton method is given by:

$$\begin{cases} x_{k+1} = x_k + \Delta x_{gn} \\ x_{k+1} = x_k - H^{-1}\nabla f \end{cases} \tag{23}$$

where ∇f and H are respectively the gradient and Hessian matrix of $\gamma(x)$ given by:

$$\begin{aligned} \nabla f &= 2J_r^T r = 2 \sum_{i=1}^m r_i \frac{\delta r_i}{\delta x_i} \\ H_{jk} &= 2J_r^T J_r = 2 \sum_{i=1}^m \left(\frac{\delta r_i}{\delta x_j} \frac{\delta r_i}{\delta x_k} + r_i \frac{\partial^2 r_i}{\partial x_j \partial x_k} \right) \end{aligned} \tag{24}$$

and therefore:

$$\Delta x_{gn} = -(J_r^T J_r)^{-1} J_r^T r \tag{25}$$

The Levenberg–Marquardt algorithm improves the iteration step size:

$$y_i = f \left(\sum_{j=1}^n w_{ij} x_j + \theta_i \right) \tag{26}$$

where I is the identity matrix and μ represents the damping factor usually having a value range of $[10^{-8}, 1]$, which ensures that $J_r^T J_r + \mu I$ is a positive definite matrix and that the iteration is in the downward direction.

Before using the neural network diagnosis, the relevant parameters of the neural network should be set according to the needs, the Sigmoid function should be selected as the activation function, the three-layer neural network should be used for training, and the other parameters should be set by default.

5. Simulation Analysis

5.1. Simulation Analysis of Winding Open-Circuit Fault

In order to verify the proposed fault diagnosis algorithm, a six-phase motor simulation model is built, which is mainly composed of a rectifier, controller, inverter, and motor. The motor parameters are: rated output power $P = 10$ kW, rated voltage $U = 311$ V, rated current $I = 20$ A, rated speed $N = 1500$ r/min, rated torque $T = 60$ N·m, pole pair $p = 5$, quadrature axis and direct axis inductance $L_d = L_q = 8.5$ mH, and power factor = 0.9.

The current waveform obtained by increasing and decreasing load and disturbance under normal conditions of the motor is shown in Figure 9. After the motor speed is increased, the load is set to 30 N·m and runs stably at 500 r/min. The six-phase stator current waveform is balanced and the sinusoidal degree is satisfactory. When the load of the motor suddenly changes to 45 N·m at 0.2 s, the current amplitude rapidly increases and runs in a stable state. When the load decreases to 40 N·m at 0.4 s, the current decreases. When the interference is added at 0.6 s, the motor current slightly increases and then decreases to the stable state.

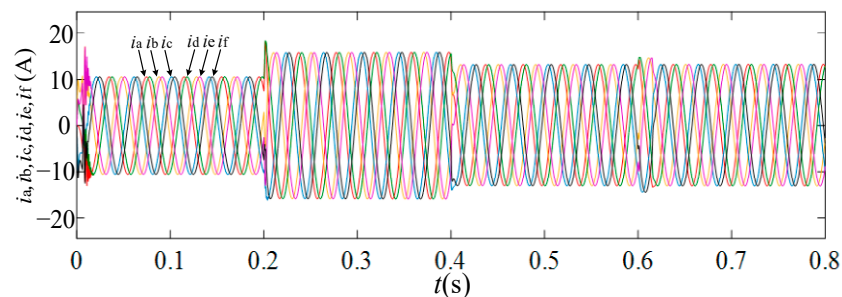


Figure 9. Current waveform of load and disturbance during normal operation.

The fault index waveform corresponding to this case is shown in Figure 10. The fault index of the six-phase open circuit is null. In addition, there is no rise when the motor stably operates, suddenly increases or decreases load, and suddenly adds disturbance. The fault index has no false diagnosis under different conditions without fault, which proves that the diagnosis method has a good robustness.

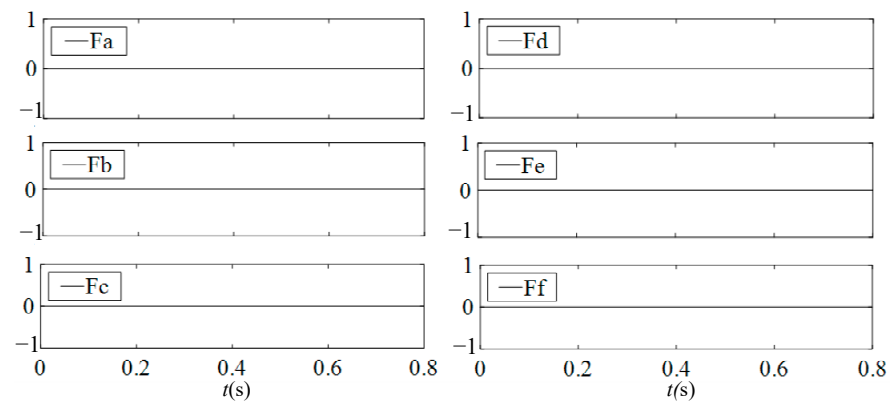


Figure 10. Fault indicators under normal operation load and disturbance.

The current waveform of the open-circuit fault of phase *a* at 0.3 s is shown in Figure 11. The load torque is 30 N·m, and the phase failure of phase *a* occurs at 0.3 s. The phase *a* current becomes zero after 0.3 s. Among the remaining four-phase currents, phase *b* and phase *c* have the same amplitude and complementary waveforms, and the waveform amplitude and phase of phase *d*, *e* and *f* change to varying degrees.

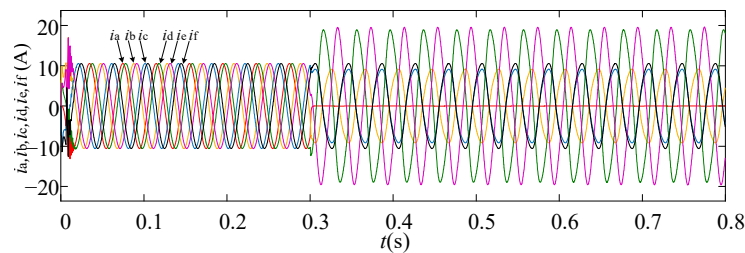


Figure 11. Phase *a* current waveform of open-circuit fault in 0.3 s.

The fault index waveform under these conditions is shown in Figure 12. After 0.3 s, the phase *a* fault index rises to 1 and the fault indexes of other phases do not change.

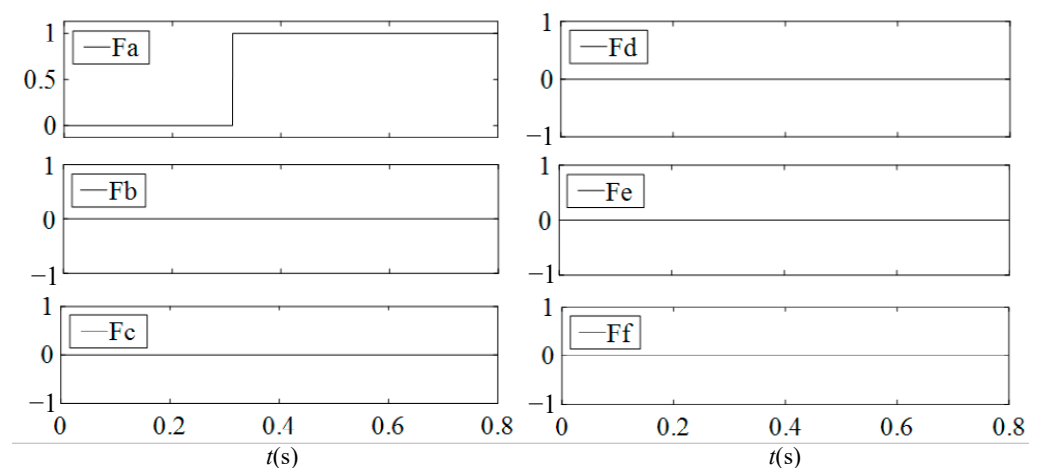


Figure 12. Phase *a* fault indicator waveform when open fault occurs within 0.3 s.

The current waveform of the open-circuit fault of phase *a* and phase *d* at 0.3 s and 0.5 s is shown in Figure 13. The load torque is 30 N·m, the phase failure of phase *a* and phase *d* occurs at 0.3 s and 0.5 s, respectively. The phase *a* current becomes zero after 0.3 s and the phase *d* current also becomes zero after 0.5 s.

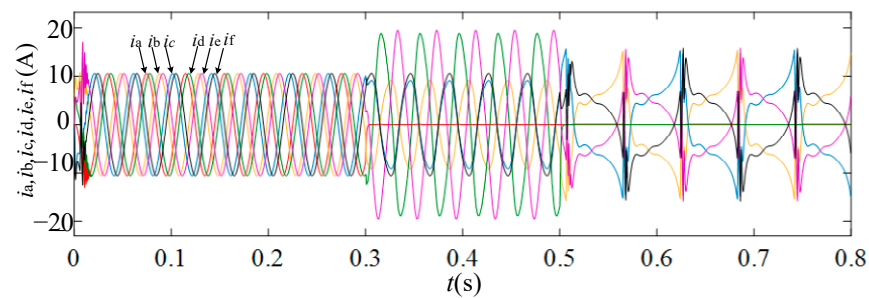


Figure 13. Current waveforms of phase *a* and phase *d* at 0.3 s and 0.5 s open-circuit fault, respectively.

The fault index waveform under these conditions is shown in Figure 14. After 0.3 s, the phase *a* fault index rises to 1, and the phase *d* fault index rapidly rises to 1 within the second half cycle of 0.5 s, so as to accurately locate the two-phase open-circuit fault.

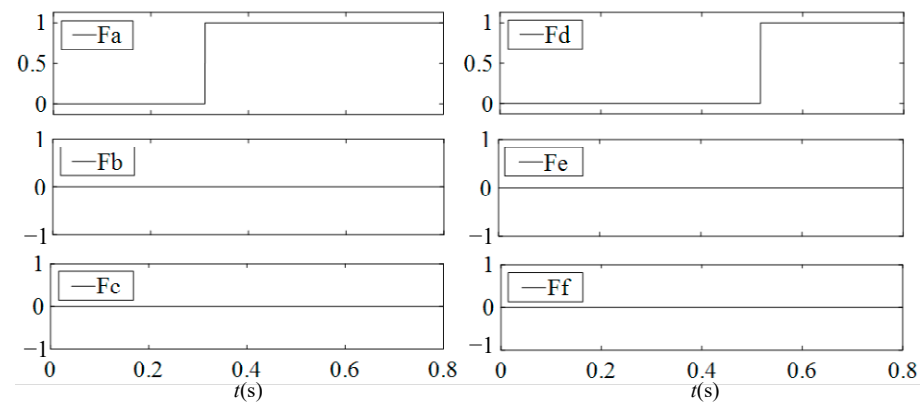


Figure 14. Fault index waveforms of phase *a* and phase *d* at 0.3 s and 0.5 s open-circuit fault, respectively.

The current waveform of the open-circuit fault of phase *a* and phase *f* at 0.3 s and 0.5 s is shown in Figure 15. The load torque is 30 N·m, the phase failure of phase *a* and phase *f* occurs at 0.3 s and 0.5 s, respectively. The phase *a* current becomes zero after 0.3 s and the phase *f* current also becomes zero after 0.5 s. Among the remaining four-phase currents, phase *b* and phase *c* have the same amplitude and opposite phase. Similarly, phase *d* and phase *e* have the same amplitude and opposite phase.

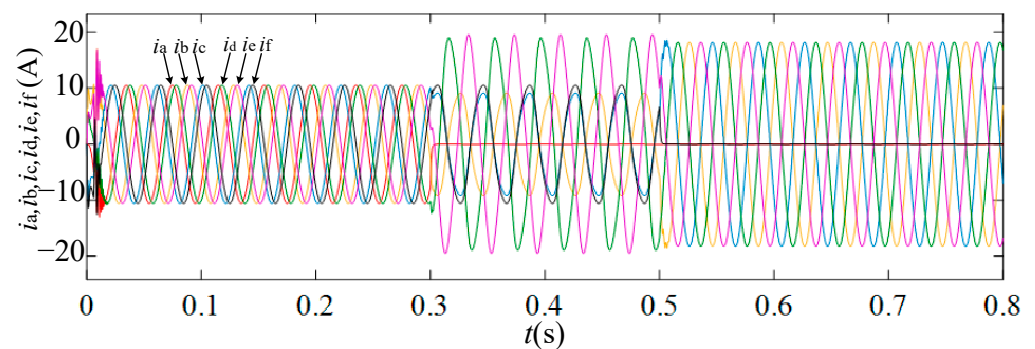


Figure 15. Current waveforms of phase *a* and phase *f* at 0.3 s and 0.5 s open-circuit fault, respectively.

The fault index waveform under these conditions is shown in Figure 16. After 0.3 s, the phase *a* fault index rises to 1, and the phase *f* fault index rapidly rises to 1 within the second half cycle of 0.5 s, so as to accurately locate the two-phase open-circuit fault.

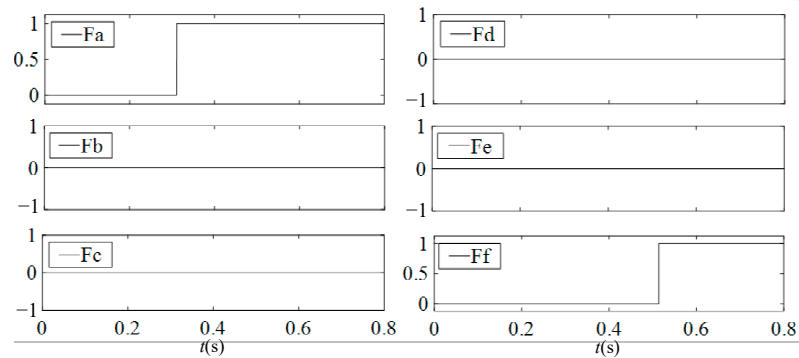


Figure 16. Fault index waveforms of phase *a* and phase *f* at 0.3 s and 0.5 s open-circuit fault, respectively.

5.2. Switch Fault Simulation

Figure 17 shows the harmonic plane current trajectories obtained by simulation in the case of 12 single-switch faults. It can be observed that the fault trajectories of the 12 switches of the six-phase VSI inverter are consistent with the theory.

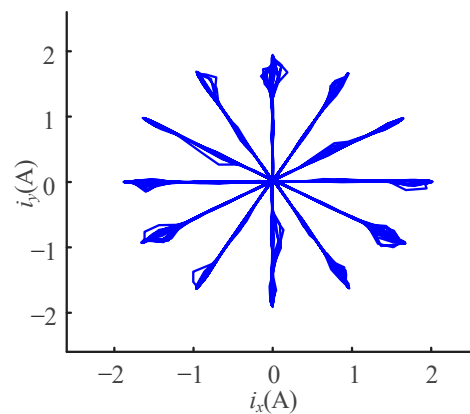


Figure 17. z_1 - z_2 harmonic plane current trace in case of single-switch fault.

Figure 18 illustrates the harmonic plane current trajectories obtained by simulation, in the case of 24 types of two-switch faults. The harmonic plane current trajectories are fan-shaped patterns with different center angles in the case of two-switch faults, that are used as characteristic signals for fault diagnosis.

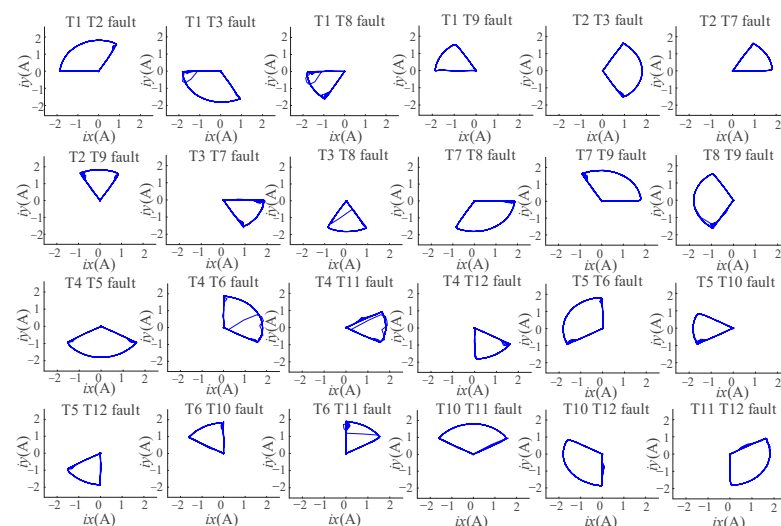


Figure 18. z_1 - z_2 harmonic plane current trace in case of two-switch fault.

Figure 19 presents the training model of the neural network. The current vector characteristic trajectories of single-switch fault and two-switch fault, are used as samples for training. The hidden layer neuron is 9, the expected error is 0.001, and the maximum number of iterations is 1000. The Newff function is used for training and the Sigmoid function is used as the activation function. The feedback process of the optimization error is performed using the L–M algorithm.

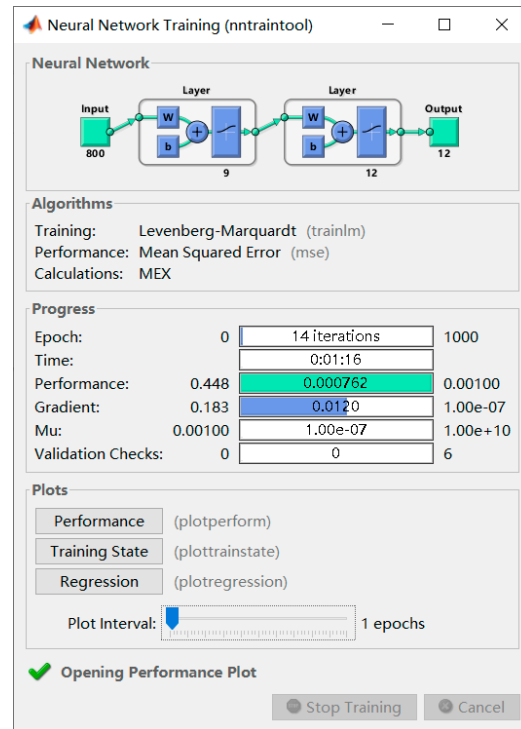


Figure 19. Neural network training model.

Figure 20 shows the training error convergence curve of the neural network. The neural network optimized using the L–M algorithm has a high convergence speed. When the training is completed 14 times, the mean square error is 7.6208×10^{-4} , which meets the error requirements.

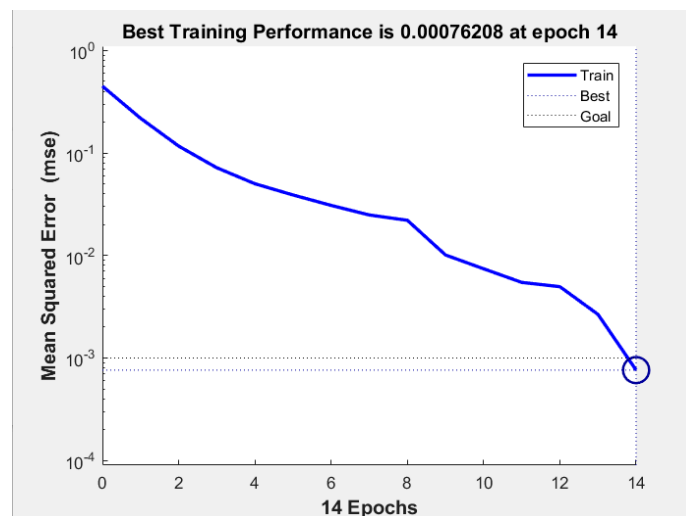


Figure 20. Error convergence curve of neural network.

The coincidence degree between the error regression curve and the expected curve shown in Figure 21 is high. This proves that the neural network has good fitting and classification ability for different fault current trajectories.

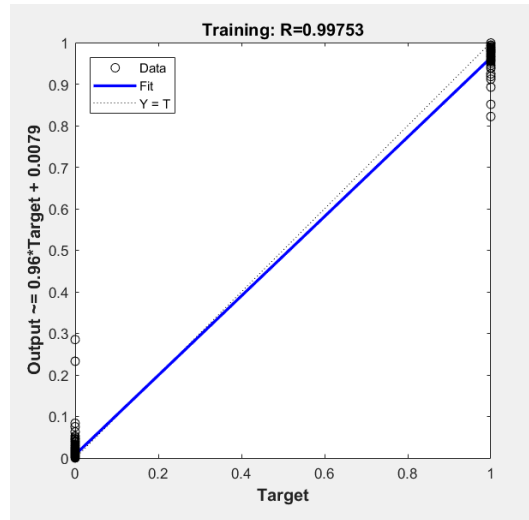


Figure 21. Regression curve of neural network training error.

The diagnosis results of the neural network are shown in Table 2. It can be seen that the trained network can identify the single-switch and two-switch faults. The error between the output value of 12 neurons in the output layer and the coding value of the fault type is very small, which leads to an accurate diagnosis.

Table 2. Neural network diagnosis results.

Serial Number	Actual Output	Ideal Output	Fault Type	
1	0.9574	0.0003	100000000000	T1
	0.0923	0.0119		
	0.0492	0.0087		
	0.0029	0.0565		
	0.0984	0.0278		
	0.0106	0.0012		
2	0.0094	0.9869	010000000000	T2
	0.0147	0.0131		
	0.0106	0.0236		
	0.0293	0.0001		
	0.0882	0.0017		
	0.0453	0.0031		
3	0.0895	0.0282	001000000000	T3
	0.9365	0.0013		
	0.0003	0.0002		
	0.0718	0.1507		
	0.0004	0.0077		
	0.0002	0.0221		
4	0.0016	0.0000	000100000000	T4
	0.0071	0.9399		
	0.0615	0.0297		
	0.0001	0.0578		
	0.0000	0.0313		
	0.0001	0.0373		

Table 2. Cont.

Serial Number	Actual Output	Ideal Output	Fault Type
5	0.0002 0.0181	000010000000	T5
	0.0001 0.0198		
	0.9987 0.0001		
	0.0003 0.0001		
	0.0000 0.0001		
	0.2961 0.0052		
6	0.0068 0.0009	000001000000	T6
	0.0001 0.0384		
	0.0000 0.9631		
	0.0064 0.0002		
	0.0103 0.0000		
	0.0200 0.0000		
7	0.0010 0.0060	000000100000	T7
	0.0217 0.0580		
	0.1198 0.0036		
	0.9840 0.0385		
	0.0447 0.0691		
	0.0316 0.0005		
8	0.1813 0.0000	000000010000	T8
	0.0052 0.0019		
	0.0398 0.0241		
	0.0077 0.9211		
	0.0005 0.0055		
	0.0000 0.0904		
9	0.0049 0.0096	000000001000	T9
	0.0003 0.0111		
	0.0893 0.0558		
	0.0040 0.0764		
	0.9695 0.1351		
	0.0002 0.0058		
10	0.0156 0.0001	000000000100	T10
	0.0099 0.0003		
	0.085 0.0324		
	0.0000 0.0054		
	0.0009 0.9973		
	0.0001 0.0237		
11	0.0000 0.0019	000000000010	T11
	0.0021 0.0021		
	0.0055 0.0009		
	0.0001 0.0000		
	0.0014 0.6796		
	0.9954 0.0058		
12	0.0137 0.0000	000000000001	T12
	0.0233 0.0171		
	0.0014 0.0001		
	0.0244 0.0005		
	0.0000 0.0001		
	0.0227 0.9101		
13	0.9455 0.9961	110000000000	T1T2
	0.0199 0.0014		
	0.0007 0.0059		
	0.0699 0.0720		
	0.0533 0.0006		
	0.0000 0.0012		

Table 2. Cont.

Serial Number	Actual Output	Ideal Output	Fault Type
14	0.9635 0.0585	101000000000	T1T3
	0.9787 0.0003		
	0.0013 0.0002		
	0.1210 0.0322		
	0.0418 0.1409		
	0.0006 0.0002		
15	0.9465 0.0002	100000010000	T1T8
	0.0262 0.0004		
	0.0414 0.0618		
	0.0002 0.9202		
	0.0022 0.0302		
	0.0000 0.0214		
16	0.9799 0.1623	100000001000	T1T9
	0.0730 0.0002		
	0.0022 0.0116		
	0.0092 0.0692		
	0.9608 0.1598		
	0.0000 0.0007		
17	0.0247 0.9807	011000000000	T2T3
	0.9339 0.0015		
	0.0016 0.0001		
	0.0754 0.0216		
	0.0840 0.0010		
	0.0391 0.0007		
18	0.0001 0.9602	010000100000	T2T7
	0.0222 0.0063		
	0.0264 0.0007		
	0.9491 0.0050		
	0.0870 0.0007		
	0.0175 0.0411		
19	0.0004 0.9792	010000001000	T2T9
	0.0095 0.0001		
	0.0016 0.0549		
	0.0009 0.0012		
	0.9561 0.0095		
	0.0141 0.0937		
20	0.0479 0.0051	001000100000	T3T7
	0.9673 0.0080		
	0.0000 0.0008		
	0.9701 0.0603		
	0.0000 0.0512		
	0.0000 0.0003		
21	0.0076 0.0000	001000010000	T3T8
	0.9344 0.0029		
	0.0003 0.0068		
	0.0003 0.9902		
	0.0001 0.0724		
	0.0958 0.0069		
22	0.0000 0.0000	000110000000	T4T5
	0.0195 0.9876		
	0.8665 0.0032		
	0.0001 0.0001		
	0.0000 0.0051		
	0.0507 0.0106		

Table 2. Cont.

Serial Number	Actual Output	Ideal Output	Fault Type
23	0.0002 0.0186	000101000000	T4T6
	0.0001 0.9968		
	0.0311 0.9535		
	0.0064 0.0002		
	0.0000 0.0000		
	0.0366 0.0000		
24	0.0000 0.0092	000100000010	T4T11
	0.0005 0.9422		
	0.0242 0.0008		
	0.0000 0.0008		
	0.0000 0.0036		
	0.9658 0.0414		
25	0.0000 0.0000	000100000001	T4T12
	0.0051 0.9606		
	0.0115 0.0004		
	0.0428 0.0034		
	0.0000 0.0009		
	0.0274 0.9119		
26	0.0002 0.0494	000011000000	T5T6
	0.0000 0.0011		
	0.8858 0.9982		
	0.0017 0.0001		
	0.0032 0.0001		
	0.0969 0.0000		
27	0.1324 0.0013	000010000100	T5T10
	0.0000 0.0000		
	0.9892 0.0006		
	0.0000 0.0357		
	0.0004 0.8010		
	0.0008 0.0048		
28	0.0001 0.0001	000010000001	T5T12
	0.0122 0.1004		
	0.9647 0.0000		
	0.0021 0.0003		
	0.0000 0.0363		
	0.0163 0.7030		
29	0.0315 0.0002	000001000100	T6T10
	0.0368 0.0010		
	0.0001 0.9669		
	0.0163 0.0004		
	0.0328 0.8387		
	0.0001 0.0033		
30	0.0000 0.0015	000001000010	T6T11
	0.0001 0.1827		
	0.0001 0.6872		
	0.0673 0.0000		
	0.0026 0.0000		
	0.9825 0.0000		
31	0.0050 0.0000	000000110000	T7T8
	0.1506 0.0274		
	0.0174 0.0003		
	0.9406 0.9372		
	0.0022 0.0685		
	0.0001 0.0021		

Table 2. Cont.

Serial Number	Actual Output	Ideal Output	Fault Type
32	0.0724 0.0930	000000101000	T7T9
	0.0004 0.0007		
	0.0014 0.0508		
	0.9778 0.1332		
	0.9280 0.0191		
	0.0000 0.0002		
33	0.0837 0.0270	000000011000	T8T9
	0.0092 0.0007		
	0.0446 0.0027		
	0.0275 0.9727		
	0.9892 0.1027		
	0.0000 0.0011		
34	0.0000 0.0000	000000000110	T10T11
	0.0401 0.0074		
	0.0001 0.0153		
	0.0005 0.0002		
	0.0005 0.9980		
	0.6568 0.1243		
35	0.0002 0.0001	000000000101	T10T12
	0.0033 0.1092		
	0.1596 0.0033		
	0.0033 0.0407		
	0.0000 0.9995		
	0.0083 0.9203		
36	0.0008 0.0044	000000000011	T11T12
	0.0451 0.0283		
	0.0005 0.0000		
	0.0014 0.0002		
	0.0000 0.0009		
	0.9609 0.9795		

6. Experimental Verification

Figure 22 shows the overall block diagram of the six-phase PMSM control system, which provides the required DC bus voltage for the inverter after rectification by a three-phase uncontrolled rectifier bridge. The DSP-28335 chip outputs the IGBT driving waveform. The resolver and current hall sensor detect the position and phase current of the motor rotor. The Labview host computer platform can receive the motor running state and fault index waveform in DSP in real time.

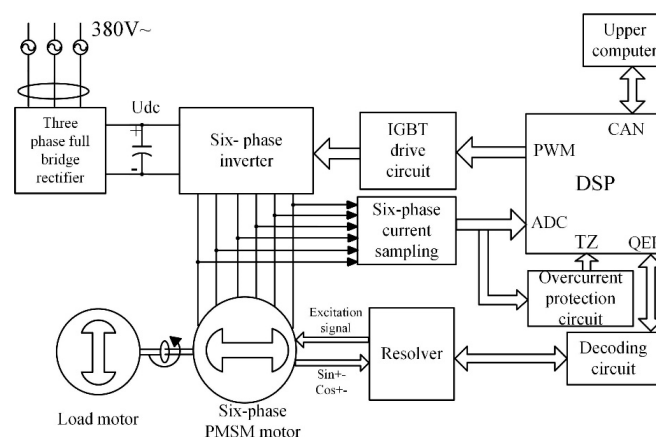


Figure 22. Overall block diagram of the six-phase PMSM control system.

In order to verify the proposed fault diagnosis algorithm, a six-phase motor experimental platform based on DSP is built. The experimental platform is shown in Figure 23. It is mainly composed of a rectifier, controller, inverter, and motor. The motor parameters are: rated output power $P = 10$ kW, rated voltage $U = 311$ V, rated current $I = 20$ A, rated speed $N = 1500$ r/min, rated torque $T = 60$ N·m, pole pair $p = 5$, quadrature axis and straight axis inductor $L_d = L_q = 8.5$ mH, and power factor = 0.94.

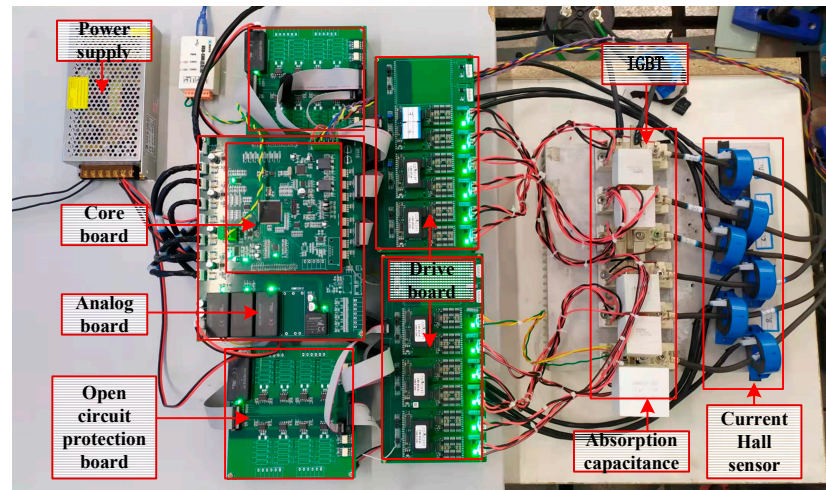


Figure 23. Experimental platform of the six-phase motor control system.

Figure 24 shows the phase current waveform when the motor is running at 500 r/min. The current is observed by collecting the voltage at the two ends of the sampling resistance. The voltage value is 100 mV, which corresponds to a current value of 2 A. The amplitudes of the phase currents are equal with a high sinusoidal degree. The current waveforms of phase a , b , and d under the same conditions are shown in Figure 24a. The phase difference between phase d current and phase a current is 30 degrees. The waveform of the motor is smooth and sinusoidal during normal operation.

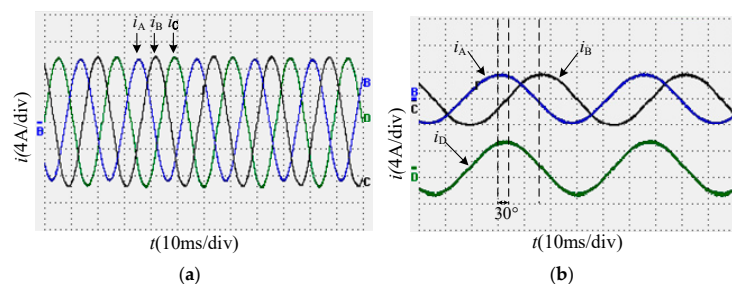


Figure 24. Waveform of motor under stable operation at 500 r/min: (a) current waveform of phase a , b , and c ; (b) current waveform of phase a , b , and d .

Figure 25 shows the motor speed and six-phase current waveform under sudden load. When the motor speed increases from 400 r/min to 500 r/min in Figure 25a, the actual motor speed gradually increases in the form of the slope with the given speed; the transition is gentle and the overshoot is small in the process of speed increase. In Figure 25b, the amplitude of the motor phase current gradually increases during loading, and the dynamic adjustment process is smooth and stable.

Figure 26 shows the motor speed and the six-phase current waveform during sudden load reduction. When the motor decelerates from 500 r/min to 400 r/min in Figure 26a, the actual motor speed gradually decreases in the form of the slope with the given speed. The transition is smooth and the overshoot is small during deceleration. In Figure 26b, the

amplitude of the motor phase current gradually decreases during load reduction, and the dynamic regulation process is smooth and stable.

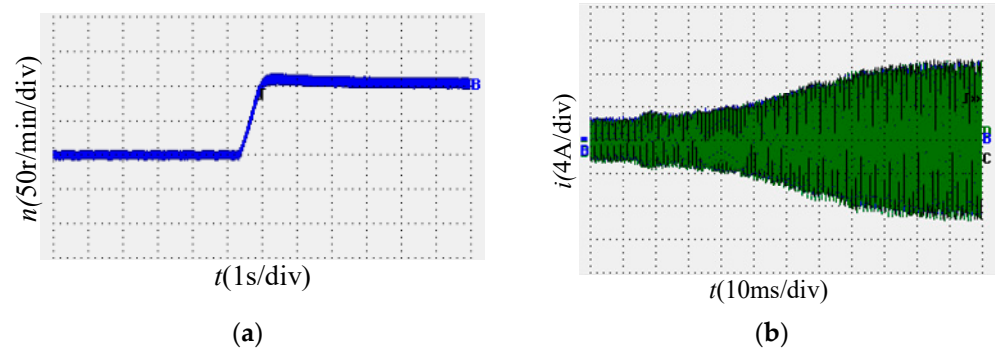


Figure 25. Waveform of the motor under sudden load: (a) speed waveform; (b) current waveform of the six-phase motor.

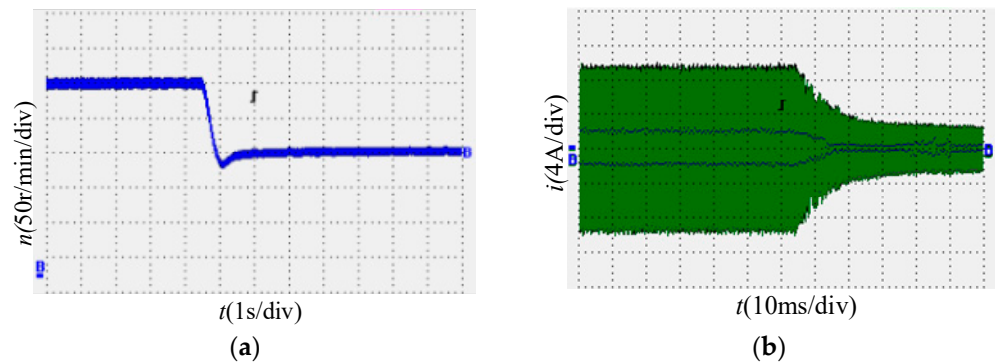


Figure 26. Waveform of the motor under sudden load: (a) speed waveform; (b) current waveform of the six-phase motor.

Figure 27 shows the fault index waveform of the motor during stable operation and sudden load increase and decrease. During stable operation and sudden load increase and decrease in the motor, the values of the six-phase open phase fault index are zero, and there is no change. The fault index has no misdiagnosis under fault-free operation, which proves that it has good robustness.

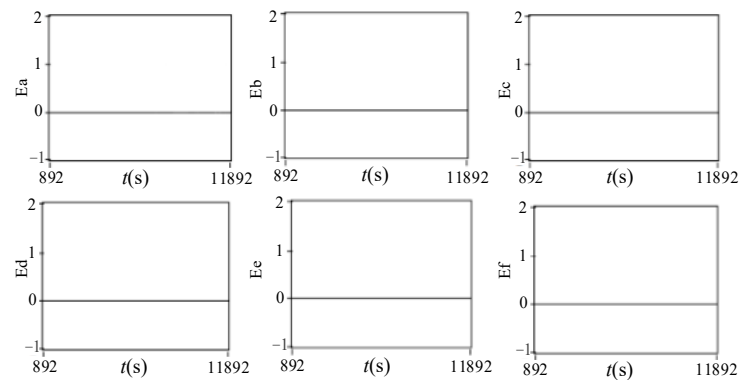


Figure 27. Fault index waveform under stable operation at 500 r/min.

Figure 28 presents the phase current and fault index waveform of motor phase *a* in the case of phase failure. Figure 28a presents the current waveform before and after the fault, in which the blue, black, and green lines respectively represent the current waveform of phase *a*, *b*, and *c* of the motor. After the phase failure of phase *a*, the current value of this phase

drops to zero, the current amplitude of phase *b* and *c* becomes almost twice the original one, and the phase positions are complementary. Figure 28b illustrates the waveform of the fault phase current and fault index. After the phase failure of phase *a*, the phase failure index E_a of phase *a* increases to a high level after 32 ms, and the optimized fault index has no obvious burr and peak pulse. Therefore, the fault diagnosis and early warning can be performed in a short time.

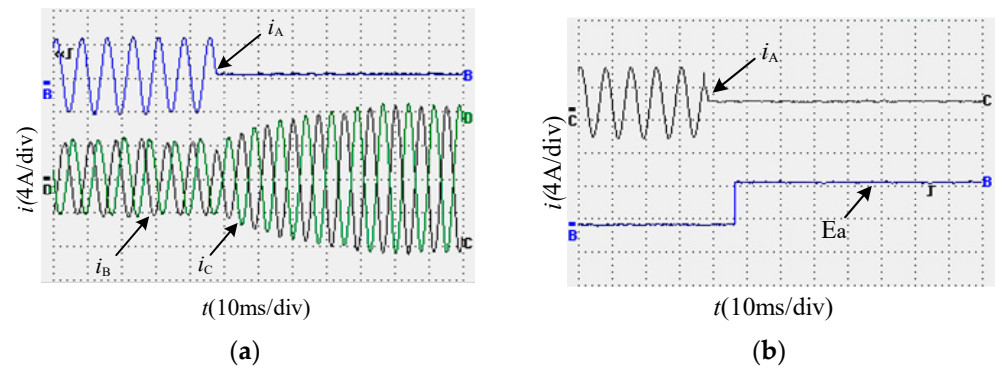


Figure 28. Phase current and fault index waveform in case of phase failure of phase *a*: (a) fault current waveform; (b) fault phase current and fault index waveform.

Figure 29 shows the fault index waveform of the six-phase disconnection when the *a* phase disconnection fault occurs. After the fault occurs, only the fault index E_a of phase *a* rises to 1, while the fault indexes of the other phases do not change, and there is no misdiagnosis.

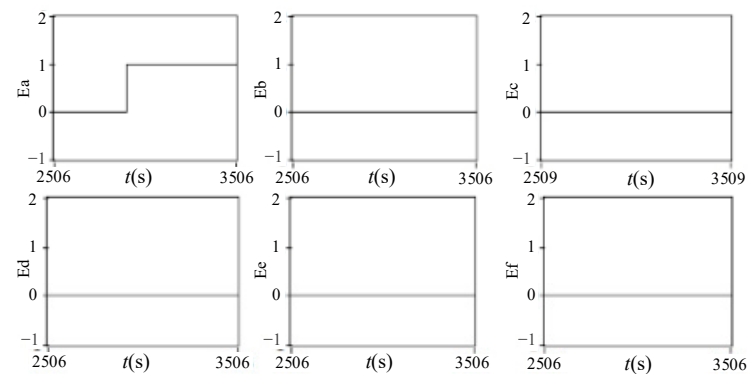


Figure 29. Fault index waveform in case of phase failure of phase *a*.

The phase current and fault index waveform of phase *a* and phase *d* of the motor with phase failure, are shown in Figure 30. The blue, black, and green lines shown in Figure 30a represent the current waveforms of motor phases *a*, *b*, and *d*, respectively. After the phase failure of phase *a* and *d*, the corresponding phase current value drops to zero, and the amplitude of the phase *b* current increases. The six-phase failure index waveform of phase *a* and phase *d* is shown in Figure 31. Before the phase failure occurs, the six-phase failure index remains null. After the failure occurs, the failure indexes E_a and E_d of phase *a* and phase *d* rise to 1, while the other four-phase failure indexes remain null without misdiagnosis.

Figure 32 shows the phase current and fault index waveform of phase failure of phase *a* and phase *f*. The blue, black, and green lines shown in Figure 32a represent the current waveforms of motor phases *a*, *b*, and *f*, respectively. A phase failure occurs in phase *a* and phase *f*, and the current value drops to zero. After the failure of phase *a* and phase *f*, their failure indexes E_a and E_f jump to the high level after 22 ms and 24 ms, respectively. These

situations show that the proposed open phase fault diagnosis method has a high diagnosis speed, and can accurately locate the fault phase position.

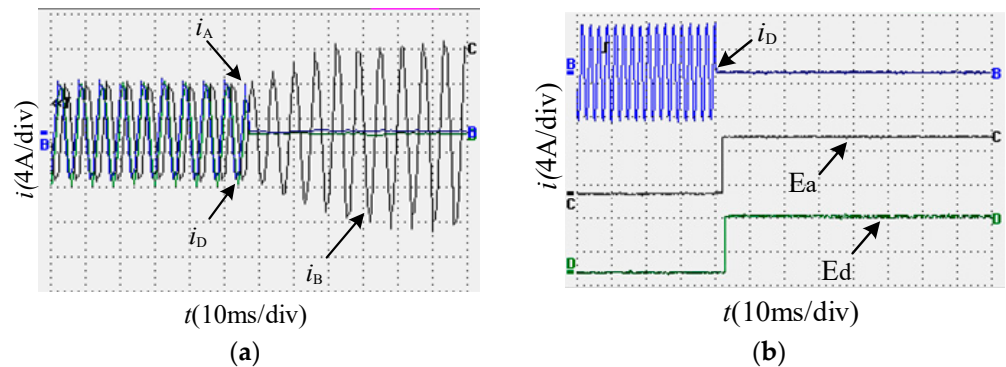


Figure 30. Phase current and fault index waveform in case of phase failure of phase *a* and phase *d*: (a) fault current waveform; (b) fault phase current and fault index waveform.

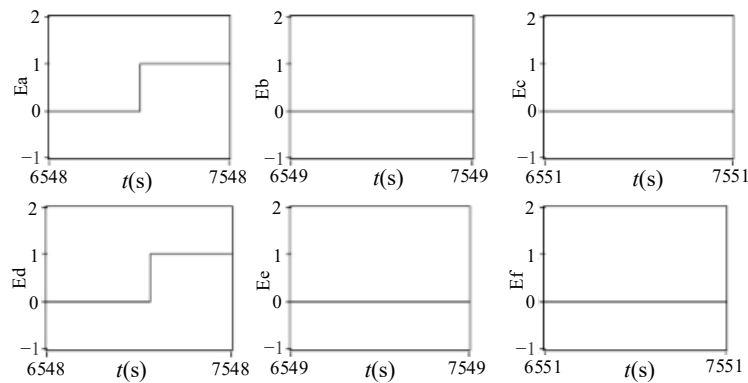


Figure 31. Fault index waveform in case of phase failure of phase *a* and phase *d*.

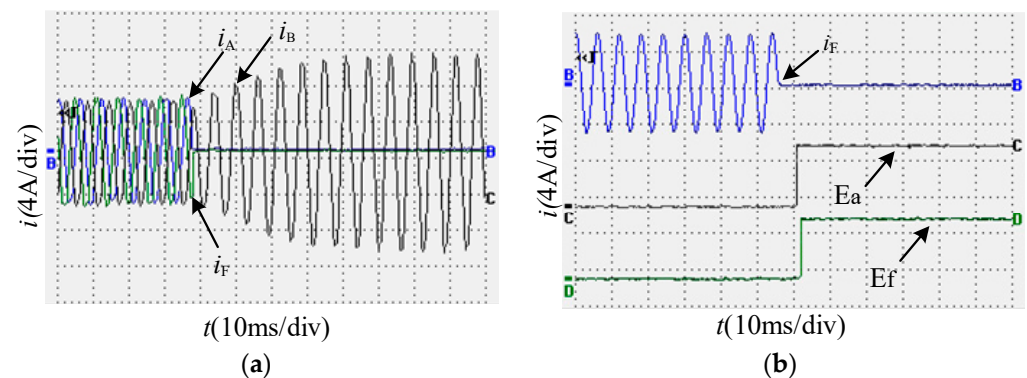


Figure 32. Phase current and fault index waveform in case of phase failure of phase *a* and phase *f*: (a) fault current waveform; (b) fault phase current and fault index waveform.

The six-phase failure index waveform of phase *a* and phase *f* is shown in Figure 33. During normal operation, the failure indexes of the two phases are 0. After phase *a* and phase *f* fail, their failure indexes E_a and E_f rise to 1, and the failure indexes of the other phases do not change. It can then be deduced that the fault index of each phase can accurately locate the position of the fault phase. In addition, the diagnosis results are accurate, and there will be no false diagnosis. Finally, the experimental results are coherent with the theoretical analysis, which verifies the correctness and efficiency of the proposed diagnosis algorithm.

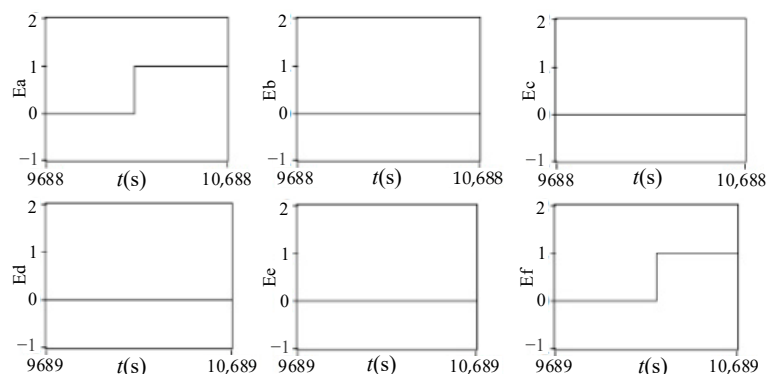


Figure 33. Fault index waveform in case of phase failure of phase *a* and phase *f*.

7. Conclusions

This paper proposed a fault diagnosis method based on vector space decoupling (VSD). The open phase fault index is derived according to the VSD inverse transformation and the current constraints after the fault. The fault index is optimized in order to prevent misdiagnosis and improve reliability. The diagnosis of a single-phase and double-phase fault can be performed in one fundamental cycle. In addition, by considering the unique harmonic plane current track after VSD transformation as the characteristic signal, a neural network is used to identify different fault current tracks, in order to diagnose the switch fault. The simulation and experimental results show that the proposed scheme has a high detection speed, ability to deal with several fault types, and good robustness. Finally, the proposed approach can accurately locate the winding open-circuit fault and power switch fault, which can be used for inverter open-circuit fault diagnosis and provides a basis for maintenance personnel.

Author Contributions: Conceptualization, H.G.; formal analysis, H.G. and J.G.; data curation, Z.H. and J.G.; writing—review and editing, B.Z. and Y.D. All authors have read and agreed to the published version of the manuscript.

Funding: This research work was funded by the National Natural Science Foundation of China grant number 51177031.

Data Availability Statement: The data presented in this study are available on request from the corresponding author.

Conflicts of Interest: The authors declare no conflict of interest.

References

1. Boglietti, A.; Cavagnino, A.; Tenconi, A.; Vaschetto, S. The Safety Critical Electric Machines and Drives in the more Electric Aircraft: A survey. In Proceedings of the 2009 35th Annual Conference of IEEE Industrial Electronics, Porto, Portugal, 3–5 November 2009; pp. 2587–2594.
2. Ma, W.M.; Wang, D.; Cheng, S.W.; Chen, J.Q. Common basic scientific problems and technological development frontier of high performance motor system. *Chin. J. Electr. Eng.* **2016**, *36*, 2025–2035.
3. Yan, M.; Ma, W.M.; Ou, Y.B.; Mang, M.Z.; Lu, L. Study on performance of dual nine phase energy storage motor system. *Chin. J. Electr. Eng.* **2015**, *35*, 6.
4. Jeong, Y.S.; Sul, S.K.; Schulz, S.E.; Patel, N.R. Fault Detection and Fault Tolerant Control of Interior Permanent Magnet Motor Drive System for Electric Vehicle. *IEEE Trans. Ind. Appl.* **2003**, *41*, 1458–1463.
5. IEEE Committee Report. Report of Large Motor Reliability Survey of Industrial and Commercial Installations. *IEEE Trans. Ind. Appl.* **1985**, *23*, 153–158.
6. Gao, H.W.; Su, J.Y.; Yang, G.J. Open circuit fault diagnosis method of five phase inverter based on pole voltage error standardization. *Chin. J. Electr. Eng.* **2016**, *36*, 10.
7. Zhang, Z.; Luo, G.A. Hybrid Diagnosis Method for Inverter Open-Circuit Faults in PMSM Drives. *China Electrotech. Soc. Trans. Electr. Mach. Syst.* **2020**, *4*, 180–189. [[CrossRef](#)]
8. Diallo, D.; Benbouzid, M.E.H.; Hamad, D.; Pierre, X. Fault Detection and Diagnosis in an Induction Machine Drive: A Pattern Recognition Approach Based on Concordia Stator Mean Current Vector. *IEEE Trans. Energy Convers.* **2005**, *20*, 512–519. [[CrossRef](#)]

9. Yang, Z.L.; Wu, Z.G.; Li, H. Open circuit fault diagnosis method of inverter based on DC side current detection. *Chin. J. Electr. Eng.* **2008**, *28*, 18–22.
10. Dabour, S.M.; Rashad, E.; Hammad, R. Open-Circuit Fault Detection of Asymmetrical Six-phase Induction Motor Fed from Z-Source Inverter. In Proceedings of the 2019 21st International Middle East Power Systems Conference (MEPCON), Cairo, Egypt, 17–19 December 2019; pp. 1216–1222.
11. Zhang, Z.; Qi, S.; Liu, X. A Diagnosis Method for Open Circuit Fault of Dual Three-Phase Permanent Magnet Synchronous Motor Drive System. In Proceedings of the 2018 21st International Conference on Electrical Machines and Systems (ICEMS), Jeju, Korea, 7–10 October 2018; pp. 1425–1430.
12. Yang, C.; Gui, W.; Chen, Z.; Zhang, J.; Peng, T.; Yang, C. Voltage Difference Residual-Based Open-Circuit Fault Diagnosis Approach for Three-Level Converters in Electric Traction Systems. *IEEE Trans. Power Electron.* **2019**, *35*, 3012–3028. [[CrossRef](#)]
13. Chen, Y.; Zhang, J.J.; Chen, Z.Y. On line diagnosis of open circuit fault of three-phase inverter circuit based on current observer. *J. Electrotech.* **2019**, *34*, 609–617.
14. Chen, C.B.; Wang, X.X.; Gao, S.; Zhang, Y.M. Open circuit fault diagnosis method of inverter based on interval sliding mode observer. *Chin. J. Electr. Eng.* **2020**, *40*, 4569–4579.
15. Danjiang, C.; Yinzhong, Y. Open circuit fault diagnosis method of three-level inverter based on multi neural network. *J. Electrotech.* **2013**, *28*, 120–126.
16. Cai, F.Y. *Research on Fault Diagnosis and Fault Tolerant Operation of Underwater Permanent Magnet Synchronous Motor Driver*; Harbin Institute of Technology: Harbin, China, 2016.
17. Zhang, X.D.; Xu, B.J.; Wu, G.X.; Zuo, Y.B. Research on wind turbine fault diagnosis expert system. *Manuf. Autom.* **2014**, *36*, 21–25.
18. Trabelsi, M.; Nguyen, N.K.; Semail, E. Real-Time Switches Fault Diagnosis Based on Typical Operating Characteristics of Five-Phase Permanent Magnetic Synchronous Machines. *IEEE Trans. Ind. Electron.* **2016**, *63*, 4683–4694. [[CrossRef](#)]
19. Zhou, C.Y.; Shen, Y.X. Open circuit fault diagnosis of double three-phase voltage source inverter based on wavelet analysis. *J. Mot. Control.* **2020**, *24*, 65–75.
20. Chen, Y.; Liu, Z.L.; Chen, Z.Y. Fast diagnosis and location method of inverter open circuit fault based on current vector feature analysis. *J. Electrotech.* **2018**, *33*, 883–891.
21. Cui, J.; Wang, Q.; Gong, C.Y. Research on inverter power tube fault diagnosis technology combined with wavelet and Concordia transform. *Chin. J. Electr. Eng.* **2015**, *35*, 3110–3116.
22. Hu, Y.; Li, Y.; Ma, X.; Li, X.; Huang, S. Flux-Weakening Control of Dual Three-Phase PMSM Based on Vector Space Decomposition Control. *IEEE Trans. Power Electron.* **2021**, *36*, 8428–8438. [[CrossRef](#)]
23. Xie, R.; Wang, X.M.; Li, Y.; Zhao, K.R. Research and application on improved BP neural network algorithm. In Proceedings of the 2010 5th IEEE Conference on Industrial Electronics and Applications, Taichung, Taiwan, 15–17 June 2010; pp. 1462–1466.
24. Cheng, H.; Cui, L.; Li, J. Application of improved BP neural network based on LM algorithm in desulfurization system of thermal power plant. In Proceedings of the 2017 Chinese Automation Congress (CAC), Jinan, China, 20–22 October 2017; pp. 5917–5920.